Static Subspace Approximation for Random Phase Approximation Correlation Energies: Applications to Materials for Catalysis and Electrochemistry

Jacob M. Clary,[†] Olivia A. Hull,[†] Daniel Weinberg,[‡] Ravishankar Sundararaman,[¶] Mauro Del Ben[†,*,‡] and Derek Vigil-Fowler[†*,†]

[†]*Materials, Chemical, and Computational Science Directorate, National Renewable Energy Laboratory, Golden, CO, USA*

[‡]*Applied Mathematics & Computational Research Division, Lawrence Berkeley National Laboratory, Berkeley, CA, USA*

[¶]*Department of Materials Science and Engineering, Rensselaer Polytechnic Institute, Troy, NY, USA*

E-mail: mdelben@lbl.gov; derek.vigil-fowler@nrel.gov

Abstract

Modeling complex materials using high-fidelity, ab-initio methods at low cost is a fundamental goal for quantum chemical software packages. The GW approximation and random phase approximation (RPA) provide a unified description of both electronic structure and total energies using the same physics in a many-body perturbative approach that can be more accurate than generalized-gradient density functional theory (DFT) methods. However, GW/RPA implementations have historically been limited

to either specific materials classes or application towards small chemical systems. The static subspace approximation allows for reduced cost full-frequency GW/RPA calculations and has previously been benchmarked thoroughly for GW calculations. Here, we describe our approach to including partial occupations of electronic orbitals in full-frequency GW and RPA calculations for the study of electrocatalysts. We benchmarked RPA total energy calculations using the subspace approximation across a diverse test suite of materials for a variety of computational parameters. The benchmarking quantifies the impact of different extrapolation procedures for representing the static polarizability at infinite screened cutoff, and shows that using screened cutoffs above 20-25 Ryd result in diminishing accuracy returns for predicting RPA total energies. Additionally, for moderately sized electrocatalytic models, 2-3 times fewer computational resources are used to compute RPA total energies by representing the static polarizability with 20-30% of the static subspace basis, with an error of approximately 0.01 eV or better in RPA adsorption energy calculations. Finally, we show that for these electrochemical models RPA can shift DFT adsorption energy shifts by up to 0.5 eV and that GW can frequently shift DFT eigenvalues of surface and adsorbate states by approximately 0.5-1 eV.

1 Introduction

The materials and catalysts needed for renewable energy applications such as fuel cells, batteries, electrolyzers, and solar cells are complex and diverse, and understanding their properties requires accurate and performant quantum chemical modeling software. Although current density functional theory (DFT) packages are mature and widely used in chemistry research,[1–7] implementations of more expensive beyond-DFT approaches, such as the GW approximation and random phase approximation (RPA), are less well developed. Such implementations typically are targeted towards certain material classes, such as semiconductors and molecules, since these tend to show larger beyond-DFT exchange-correlation effects due

to reduced electronic screening.[8–10] Additionally, many beyond-DFT software packages scale poorly to large system sizes due to parallelization limitations and the well-known nominal quartic dependence of the computational resources needed on the system size (at minimum). Despite these issues, the ab-initio accuracy improvement of RPA and GW in describing, on average, molecular reaction energies, lattice constants, surface adsorption, and electronic structures in comparison to generalized-gradient DFT methods is appealing and been a major driver of their continued development.[11]

Electrocatalysts provide an interesting challenge to beyond-DFT methodologies because they are composed of catalysts that can be metallic,[12,13] semimetallic,[14–17] or semiconducting,[18] and they are in contact with molecules. Accurate electronic structure and total energy descriptions of (semi)metallic catalysts, along with any adsorbates present, requires beyond-DFT exchange-correlation effects within a framework that can treat partially occupied electronic orbitals. Realistic models of electrocatalytic surfaces also commonly require significantly larger computational models[19–22] relative to studies of simpler solid materials that are periodic in three dimensions. For example, the number of atoms in the slab model may be large so that adsorbate coverage effects can be studied, while vacuum/solvent space at least as wide as the surface model is used to prevent unphysical interactions in the aperiodic supercell direction. Together, these effects can increase the cost of surface calculations by at least an order of magnitude. This increased cost requires highly efficient and parallel software, and can greatly benefit from modern, GPU-based supercomputers.[23,24]

The BerkeleyGW computational package has been shown to scale well well to systems with thousands of atoms, take advantage of modern GPU computing resources, and provide an excellent platform for RPA, GW, and Bethe-Salpeter equation calculations.[25,26] Historically, BerkeleyGW algorithmic improvements that further reduce the cost of GW approximation calculations have focused on implementations that enable the study of semiconducting materials. For example, the static subspace approximation has been shown to dramatically reduce the cost of full-frequency GW calculations by using the eigenvectors of the static

polarizability to efficiently represent the polarizability at other frequencies in place of the full basis of reciprocal lattice vectors.[27] However, this approach has not been benchmarked for metallic systems with partially occupied orbitals nor for calculating RPA total energies.

In insulating materials, the orbital occupations are defined by a step function at 0 K such that states below the Fermi level have an occupation of 1 while states above the Fermi level have an occupation of 0. In contrast, metallic systems do not have a band gap, but instead have one or more bands that cross the Fermi level. Consequently, implementations of quantum chemical methods involving the numerical integration of the Brillouin zone on a **k**-point grid in reciprocal space,[28] as is common in periodic DFT and beyond-DFT software packages, must account for these partially occupied bands in metallic systems. Without introducing temperature, converging such calculations typically involves the use of a very fine **k**-point grid.[29–31] A widely used alternative approach to dense sampling involves using occupations that are not exactly equal to 0 or 1 in the computational formalism. The step occupation function is replaced with a function that smoothly varies from 1 to 0 as it crosses the Fermi level, thus removing the numerical challenges associated with the Brillouin zone integral discontinuity. DFT and beyond-DFT packages typically implement the same small set of continuous occupation function options based on the Fermi-Dirac occupation function, the Gaussian function, and other more complicated functions. The first-order Methfessel-Paxton scheme (MP1)[32] in particular is popular because it has been shown to yield converged total energies and other properties accurately and with the lowest computational expense, and is the approach used in this work.[33]

In this work we analyze and benchmark the effect of partial occupations and the static subspace approximation on RPA and GW calculations, demonstrating that our implementation enables accurate GW and RPA calculations for a variety of systems, including metals, at scale. To this end, we first briefly detail our method developments within the BerkeleyGW code that decrease the computational demands of RPA and GW, which include the implementation of partial occupations into the computation of the RPA polarizability and the

self-energy operator, and the implementation of the static subspace approximation to the RPA polarizability. Then, we explore the convergence behavior of RPA total energies with respect to key computational parameters for both a diverse test suite of materials and a number of (electro)catalytically relevant systems, including the size of the static subspace, the screened cutoffs used in the RPA extrapolation, **k**-point grid density, and partial occupation broadening.

2 Theory

2.1 Partial occupations in χ^0 and RPA total energies

In a plane-wave basis, the irreducible polarizability can be written as[34]

$$\chi^0_{\mathbf{G},\mathbf{G}'}(\mathbf{q},\omega) = \frac{1}{V}\sum_{\mathbf{k}}\left(\sum_{v}^{\text{val}}\sum_{c}^{\text{cond}}\left[M^{\mathbf{G}}_{vc\mathbf{k}}(\mathbf{q})\right]^*\Delta_{vc\mathbf{k}}(\mathbf{q},\omega)M^{\mathbf{G}'}_{vc\mathbf{k}}(\mathbf{q})\right. \tag{1}$$

with

$$M^{\mathbf{G}}_{nn'\mathbf{k}}(\mathbf{q}) \equiv \langle\psi_{n\mathbf{k}+\mathbf{q}}|e^{i(\mathbf{q}+\mathbf{G})\cdot\mathbf{r}}|\psi_{n'\mathbf{k}}\rangle\,, \tag{2}$$

and

$$\Delta_{vc\mathbf{k}}(\mathbf{q},\omega) = \begin{cases} g_{\mathbf{k}}(f_{c,\mathbf{k}} - f_{v,\mathbf{k}+\mathbf{q}})\left(\frac{1}{\epsilon_{n',\mathbf{k}}-\epsilon_{n,\mathbf{k}+\mathbf{q}}-\omega} + \frac{1}{\epsilon_{n',\mathbf{k}}-\epsilon_{n,\mathbf{k}+\mathbf{q}}+\omega}\right) & \epsilon_v < \epsilon_c \\ \emptyset & \epsilon_v \geq \epsilon_c \end{cases}. \tag{3}$$

Here, **k** and **q** are vectors in the first Brillouin zone, **G** and **G′** are reciprocal lattice vectors, $g_{\mathbf{k}}$ is **k**-point weight, ω is frequency, f is the state occupation, $\psi_{n\mathbf{k}}$ and $\varepsilon_{n\mathbf{k}}$ are the Kohn-Sham (KS) orbitals and energies from the DFT starting point, V is the volume of the simulation cell, and v and c count fully+partially occupied and fully+partially unoccupied bands, respectively. We have used time-reversal symmetry to reduce the double summation over all states in the Adler-Wiser formulation to a double sum in which one sum is over conduction states and the other is over valence states (generalized so both contain partially occupied states),[35] as is common in GW and RPA implementations.

In this work, all occupation factors are obtained from the 1st order Methfessel-Paxton (MP1) functional form

$$f(\varepsilon) = \frac{1}{2}(1 - \mathrm{erf}(x)) - \frac{x}{2\sqrt{\pi}} e^{-x^2}, \tag{4}$$

where $x = \frac{\varepsilon - E_f}{2\sigma}$, E_f is the Fermi energy, and $\sigma = k_B T$ is the broadening, with k_B being the Boltzmann constant.

To classify a band as fully occupied, partially occupied, or fully unoccupied, we define an energy window and label the band based on its location relative to this window, as shown in Figure 1. We define the smearing window such that any band whose occupation f falls within $10^{-6} < f < 1 - 10^{-6}$ is considered partially occupied. Consequently, occupations less than 0 (greater than 1), as can occur using MP1 broadening, are counted as fully unoccupied (occupied). We note that if a band is fully occupied or unoccupied at some **k**-points but partially occupied at others, it is counted as partially occupied.

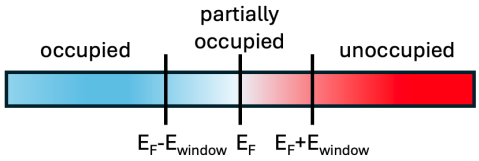

Figure 1: Schematic of $f(\varepsilon)$ and visualization of the partially occupied window. Blue corresponds to fully occupied orbitals and red corresponds to fully unoccupied orbitals. The gradient between red and blue represents the partially occupied states. The function used to determine this smooth transition between occupied and unoccupied can be chosen as Eq. 4 inside the code.

An RPA total energy, E^{RPA}, for a system can be calculated for KS orbitals as

$$E^{RPA} = F^{DFT} - E_{XC} + E_X + E_{corr}^{RPA}, \tag{5}$$

where E_{XC} is the DFT exchange-correlation energy, E_X is the exchange energy as defined in Eq. 8 below, and E_{corr}^{RPA} is the RPA correlation energy. The exact exchange energy is the Hartree-Fock energy on KS orbitals, written as $E_{XX} = E^{DFT} - E_{XC} + E_X$. The DFT

Helmholtz energy, F^{DFT}, is calculated as $F^{DFT} = E^{DFT} - TS_{occ}$, with E^{DFT} being the DFT internal energy, T the temperature, and S_{occ} the entropy introduced due to the use of partial occupations. E_{corr}^{RPA} is calculated from the irreducible polarizability using the adiabatic connection fluctuation-dissipation theorem (ACFDT) formalism as

$$E_{corr}^{RPA} = \int_0^\infty \frac{d\omega}{2\pi} \mathrm{Tr}\{\ln[1 - \chi^0(i\omega)\nu] + \chi^0(i\omega)\nu\}. \tag{6}$$

It has been previously shown that a fully nonlocal exchange-correlation functional can approximate the exact ACFDT exchange-correlation energy.[36] The exchange and correlation parts can be separated such that at zero coupling strength,[36,37] the exchange energy, E_X, can be written as

$$E_X = -\frac{e^2}{2} \int d^3\mathbf{r} d^3\mathbf{r}' \frac{1}{|\mathbf{r} - \mathbf{r}'|} \left[n(\mathbf{r})\delta(\mathbf{r} - \mathbf{r}') + \frac{1}{\pi} \int_0^\infty d\omega \chi^0(\mathbf{r}, \mathbf{r}', i\omega) \right], \tag{7}$$

with χ^0 given by the occupation-dependent polarizability in Eq. 1. The frequency integral can be evaluated analytically based on the location of the poles of χ^0, as discussed by Harl, Schimka, and Kresse.[37] Rearranging the resulting occupation factors, we can write the exchange energy as

$$E_X = \frac{-e^2}{2} \sum_{\mathbf{k}\mathbf{q}nn'} \left(\sum_{\mathbf{G}} v(\mathbf{q} + \mathbf{G}) \left| M_{nn'}(\mathbf{k}, \mathbf{q}, \mathbf{G}) \right|^2 \right) \left[\left(f_{n'\mathbf{k}} f_{n\mathbf{k}+\mathbf{q}} + \begin{cases} f_{n\mathbf{k}+\mathbf{q}}(1 - f_{n'\mathbf{k}}), & \varepsilon_{n'\mathbf{k}} < \varepsilon_{n\mathbf{k}+\mathbf{q}} \\ f_{n'\mathbf{k}}(1 - f_{n\mathbf{k}+\mathbf{q}}), & \varepsilon_{n'\mathbf{k}} > \varepsilon_{n\mathbf{k}+\mathbf{q}} \end{cases} \right) \right. \tag{8}$$

Note that the reciprocal space sum in parenthesis is just the Coulomb self energy of the pair density of states $n'\mathbf{k}$ and $n\mathbf{k} + \mathbf{q}$, and the above is equal to the exchange energy in Hartree-Fock theory, except for the second occupation factor term in brackets above. That term contributes only when both states are partially occupied, because the lower eigenvalue contributes $(1 - f)$ while the higher eigenvalue contributes f. (Also note that the combi-

nation in brackets simplifies to the f corresponding to $\max(\varepsilon_{n'\mathbf{k}}, \varepsilon_{n\mathbf{k}+\mathbf{q}})$, while the form in Eq. (8) emphasizes the correction with respect to the regular Hartree-Fock energy.) We have implemented this RPA variant of the exchange energy in JDFTx,[38] sharing implementation with the standard exchange energy for hybrid functionals,[39] with just the occupation factors modified as above.

The size of χ^0 for a calculation is determined by the number of $\mathbf{G}$-vectors with an energy less than the chosen screened cutoff, E_{screen}. These RPA-ACFDT correlation energies are known to converge slowly with respect to E_{screen}. However, the functional form of this dependence is frequently modeled at high $\mathbf{G}$ by the free electron response function, which is known to be the Lindhard function

$$E_{corr}^{RPA}(E_{screen}) = E_{corr}^{RPA,\infty} + \frac{A}{E_{screen}^{3/2}}, \tag{9}$$

where A is a fitting constant and $E_{corr}^{RPA,\infty}$ is the RPA correlation energy extrapolated to infinite screened cutoff used for calculating RPA total energies in Eq. 5.[37]

2.2 Partial occupations in GW

The GW approach solves the Dyson equation for the quasiparticle (QP) energies and wavefunctions,[40]

$$\left[-\frac{\nabla^2}{2} + V_{ion} + V_H + \Sigma(E_{nk}^{\mathrm{QP}})\right]\psi_{nk}^{\mathrm{QP}} = E_{nk}^{\mathrm{QP}}\psi_{nk}^{\mathrm{QP}}, \tag{10}$$

where ∇ is the kinetic energy operator, V_{ion} is the ionic potential, V_H is the Hartree potential, Σ is the nonlocal, energy-dependent self energy within the GW approximation, and $\mathrm{E}_{nk}^{\mathrm{QP}}$ and ψ_{nk}^{QP} are the quasiparticle energies and wavefunctions, respectively. Equation 10 is in Hartree atomic units. In the GW formalism, G refers to the one-body Green's function and W the dynamically screened Coulomb interaction used to construct Σ. We use the single-particle wavefunctions from DFT as our quasiparticle wavefunctions (the diagonal approximation).

In equation 10, the self-energy operator $\Sigma(E_{nk}^{QP})$ can be expressed within the contour-

deformation formalism as[41]

$$\Sigma(\omega) = \frac{i}{2\pi} \oint \mathrm{d}\omega' G(\omega + \omega') W(\omega') - \frac{1}{2\pi} \int_{-\infty}^{\infty} \mathrm{d}\omega' G(\omega + i\omega') W(i\omega'), \tag{11}$$

where the second term is the integral along the imaginary axis, and the first term is the contour integral in Figure 2, discussed further below. In this work, we use the non-interacting Green's function and screened Coulomb interaction, G_0 and W_0, in equation 11.

W_0 is calculated using

$$W_{0,\mathbf{GG'}}(\mathbf{q};\omega) = \epsilon^{-1}_{\mathbf{GG'}}(\mathbf{q};\omega) v(\mathbf{q}+\mathbf{G'}), \tag{12}$$

where v is the bare Coulomb interaction and ϵ is the full-frequency dielectric matrix. Within the random phase approximation[42–44] ϵ is given by

$$\epsilon_{\mathbf{GG'}}(\mathbf{q};\omega) = \delta_{\mathbf{GG'}} - v(\mathbf{q}+\mathbf{G}) \chi^0_{\mathbf{GG'}}(\mathbf{q};\omega). \tag{13}$$

In the equation above, χ^0 is the irreducible polarizability from equation 1.

The expression for the non-interacting Green's function, G_0, with partial occupations is given by[45]

$$G_0(\omega) = \lim_{\eta \to 0} \sum_s \psi_s \psi_s^* [\frac{1 - f_s}{\omega - (\epsilon_s - i\eta)} + \frac{f_s}{\omega - (\epsilon_s + i\eta)}], \tag{14}$$

where f_s is the occupation and ε_s is the Kohn-Sham energy corresponding to ψ_s. Here, we have suppressed the crystal momentum index $\mathbf{k}$, where $s = n\mathbf{k}$, and the spatial dependence for simplicity.

Application of the Sokhotski–Plemelj formula to Eq.14 yields

$$\text{Im } G_0(\omega + \omega') = i\pi \sum_s \psi_s \psi_s^* [-(1 - f_s)\delta(\omega' - (\epsilon_s - \omega)) + f_s \delta(\omega' - (\epsilon_s - \omega))]. \tag{15}$$

Note that at $T = 0$, the two pole terms in Eq. 15 collapse into a single term dictated by $\mathrm{sgn}(E_f - \epsilon_s)$, or in other words, whether or not the band is valence or conduction:

$$\mathrm{Im}\ G_{0,T=0}(\omega + \omega') = i\pi \sum_s \psi_s \psi_s^* [\mathrm{sgn}(E_f - \epsilon_s)\delta(\omega' - (\epsilon_s - \omega))] \tag{16}$$

In the $T \geq 0$ case, we can visualize the contour and poles as shown in Figure 2 (adapted from Figure 13 in Ref. 41, which shows the $T = 0$ case). The poles of G_0 appear both above and below the real axis, and are weighted by the occupation factor f_s (occupied states) or 1-f_s (unoccupied states). The larger the value of the either f_s or 1-f_s, the darker the pole coloring and the higher its weight. The partial occupations enter into the screened coulomb interaction through the irreducible polarizability.

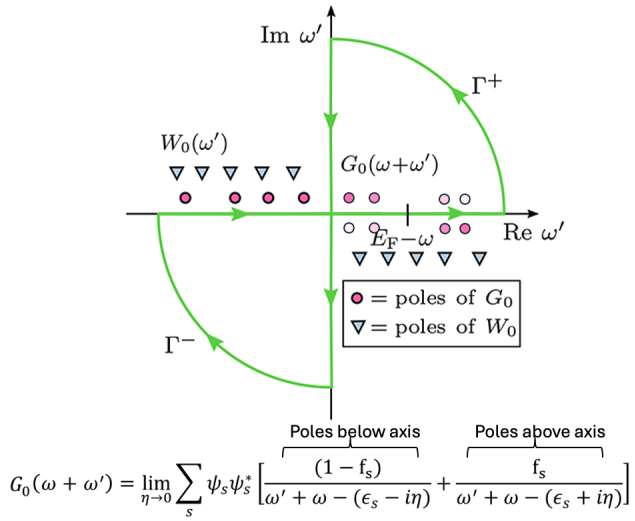

Figure 2: Visualization of the contour and poles for the self-energy operator within the contour deformation formalism with occupation factors explicitly considered (figure adapted from Ref. 41). The more lightly colored the pole, the smaller the value of the occupation factor (f_s for occupied states, 1-f_s for unoccupied states)

The inclusion of partial occupations using the above method is straightforwardly applicable to the evaluation of the GW electronic structure and RPA correlation energy using the static subspace approximation.[27] Within this approach, the evaluation of the frequency dependence part of the polarizability (as needed for the integration over the imaginary axis of equation 6) is calculated using a compressed basis obtained from the low rank approximation

of the static ($\omega = 0$) polarizability.[10,46–49] The new basis of size N_b is obtained by applying a selection criterion that determines whether a particular eigenpair should be retained. The eigenvectors selected in this way define the subspace basis used to evaluate $\chi^0(\omega)$ for ($\omega \neq 0$). This is achieved by projection of the $M_{nn'}(\mathbf{k}, \mathbf{q}, \mathbf{G})$ transition matrix elements of equation 2 from their original plane-wave basis onto the subspace basis. If N_G is the original plane-wave basis size used for the expansion of χ^0, the evaluation of its associated frequency dependent part is sped up by a factor proportional to $(N_G/N_b)^2$. We note that the χ^0 basis set size used for RPA calculations here was defined using each screened cutoff used in the Eq. 9 extrapolation, which is less than the planewave cutoff used in the DFT calculation.

3 Computational Details

Unless noted otherwise, DFT calculations were performed with the JDFTx code[38] using a 60 Ryd planewave cutoff, SG15 ONCV norm-conserving pseudopotentials,[50] and the Perdew-Burke-Ernzerhof (PBE) generalized gradient approximation (GGA) functional.[51] All calculations for the metallic systems used 1st order Methfessel-Paxton 1$^{\text{st}}$ order broadening with a broadening width of 0.2 eV, while the layered materials FeN_4@G and 1T-MoS_2 used a broadening width of 0.002 eV.[32] A summary of the system sizes and the $\mathbf{k}/\mathbf{q}$-grids used for the RPA energy benchmarking results and application materials in section 4.4 are provided in Tables S1 and S2. The bulk solid AlN (conventional wurtzite and primitive zinc blende), MgO (conventional rock salt), InP (primitive zincblende), Si (primitive diamond-structured), Na (primitive bcc), Pd (primitive fcc), and Pt (primitive fcc) unit cell lattice vectors and ions were fully relaxed using the PBE functional. Vacuum space was added to create the surfaces such that each slab width plus any adsorbates was less than half the length of each z lattice vector. For the Pt(111), MgO(001), 1T-MoS_2, and FeN_4@G systems this was approximately 15, 15, 15, and 12 Å of vacuum. The atom and molecule calculations were performed in a $10.0 \times 10.1 \times 10.2$ Å box at the Γ point. Unless noted otherwise, all molecules were relaxed

using PBE. The reference energies for single atoms were calculated using the same methodology as the molecules and with spin states shown in Table S3. For the surfaces, Coulomb truncation was applied along the z axis, which was perpendicular to each surface.[39] For the atoms and molecules, Coulomb truncation was applied along the x, y, and z axes. The lower two layers of the MgO(001) and Pt(111) surfaces were frozen for ionic optimizations. Only the x and y lattice vectors of the clean 1T-MoS_2 and FeN_4@G surfaces were allowed to relax, and were frozen for adsorption calculations. The final relaxed structures for the systems used in this work are provided as separate structures files in CIF format.

RPA and GW calculations were performed on the PBE wavefunctions with the BerkeleyGW[25] code with Coulomb truncation along the same lattice vectors as for the DFT calculations. The RPA screened cutoff set used was 17-22 Ryd. Additional details about the RPA frequency grid used and errors due to number of imaginary frequencies used are discussed in the Supporting Information and shown in Figure S1. Briefly, we used a more conservative 16 imaginary frequencies for the benchmarking calculations in this work, and 12 imaginary frequencies for the RPA surface calculations in section 4.4. The GW calculations were performed using a screened cutoff of 25 Ryd and all possible bands in the epsilon summation by efficiently representing Kohn-Sham states using the stochastic pseudobands approach.[52–54] The Cu GW quasiparticle eigenvalue calculation was performed using the bulk fcc primitive cell at its experimental lattice constant of 3.61 Å. A subspace basis set size of 100 and all possible bands up to the planewave cutoff (609) were included to facilitate comparison with literature.[27]

4 Results

The convergence of RPA total energies is dependent on DFT total energies, DFT wavefunctions, the exact exchange energy, and RPA correlation energies. The convergence of DFT calculations is well-understood, and many works discussing relevant parameters have been

published.[33,55,56] Calculations quantifying how RPA total energies converge with respect to a variety of interrelated computational parameters have been previously published, which are notably based on DFT results using projector augmented-wave (PAW) pseudopotentials.[37,57] In this work, we performed similar benchmarking for DFT results calculated using the SG15 ONCV pseudopotential[50] set and the implementation of the above approach in BerkeleyGW.[23,25,53] Here, we highlight how broadening, $\mathbf{k}/\mathbf{q}$-grid, the screened cutoff extrapolation, and the static subspace approximation impact RPA total energies because they are most directly tied to the new implementation described above. We also demonstrate the application of our approach to systems relevant to (electro)catalysis.

4.1 Effect of broadening and k/q-grid

Figure 3 shows that our implemented broadening scheme results in bulk solid Na RPA total energies that are stable with respect to both MP1 broadening width and $\mathbf{k}/\mathbf{q}$-grid. We note that for each set of points along the x-axis in the left subplot, the same $\mathbf{k}/\mathbf{q}$-grid was used for the DFT calculation, E_{XX} calculation, and RPA calculation. These results are in excellent agreement with similar calculations in literature.[37] The left subplot shows that although the Na E_{corr}^{RPA} and E_{XX} energy terms converge in opposite directions with respect to $\mathbf{k}/\mathbf{q}$-grid, when added together as RPA total energies this dependence largely cancels such that the total RPA energy is much more stable than either of its constituent quantities. The solid vs. dashed lines show that this behavior is similar for two different broadening widths. Similarly, the right subplot shows that different MP1 broadening widths do not significantly change the convergence behavior of the bulk Na RPA total energy from the DFT total energy. Finally, we note similar behavior for bulk Pt (Figure S2). Overall, these results indicate that using a $\mathbf{k}/\mathbf{q}$-grid equivalent to a 12×12×12 $\mathbf{k}/\mathbf{q}$-grid for these bulk metals with primitive unit cells and 0.2 eV MP1 broadening width will yield reliable RPA total energies for metallic systems and use these settings for all results in this work.

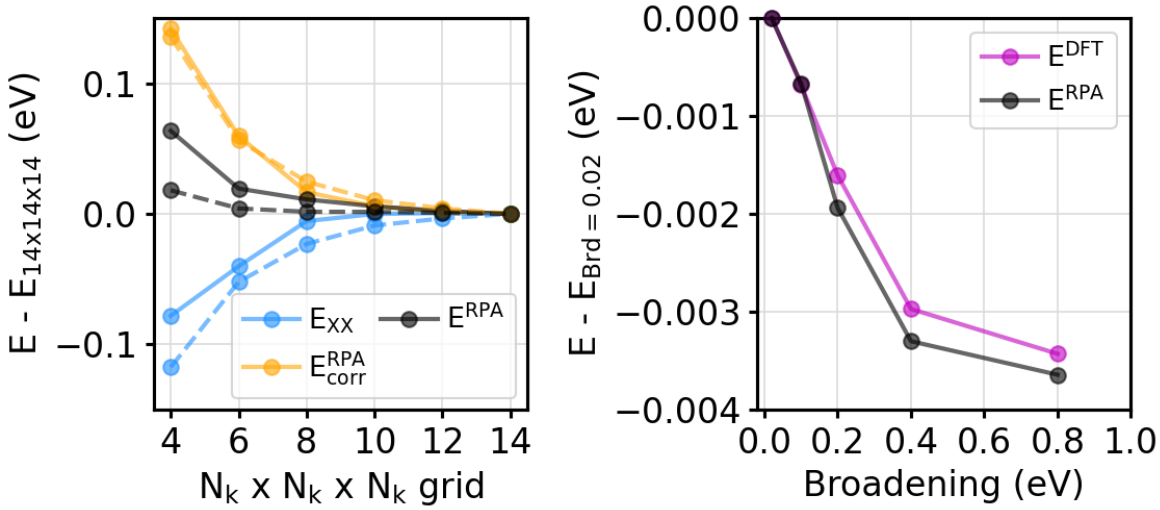

Figure 3: (Left) Impact of $\mathbf{k}/\mathbf{q}$-grid on Na E_{XX}, E_{corr}^{RPA}, and E^{RPA}. Energies shown as solid (dashed) lines were calculated using an MP1 broadening width of 0.2 (0.8) eV. All energies are shown relative to their value calculated using a 14×14×14 $\mathbf{k}/\mathbf{q}$-grid. For each set of points along the x-axis, the same $\mathbf{k}/\mathbf{q}$-grid was used for the DFT calculation, E_{XX} calculation, and RPA calculation. (Right) Change in Na E^{DFT} and E^{RPA} as a function of the MP1 broadening width. All energies are shown relative to their value calculated using an MP1 broadening width of 0.02 eV. All energies were calculated using a 12×12×12 $\mathbf{k}/\mathbf{q}$-grid.

4.2 Screened cutoff extrapolation for RPA total energies

Previous work found that RPA correlation energy extrapolations using PAW pseudopotentials produced accurate results using 8 screened cutoffs with energies approximately 50-66% of the PAW planewave cutoff.[37] However, to our knowledge, similar calculations using the SG15 pseudopotential set, which might be most accurate using different screened cutoffs, have not been performed. One important choice in RPA methodology involves the construction of χ^0. The set of $E_{corr}^{RPA}(E_{screen})$ used in each final RPA extrapolation (left-hand side of Eq. 9) could be calculated from χ^0 constructed using bands with kinetic energy less than either: 1) each screened cutoff such that the conduction band index (c-index) in Eq. 1 counts more unoccupied bands for the larger screened cutoffs, or 2) the planewave cutoff such that the c-index in Eq. 1 remains constant for different screened cutoffs.

The RPA atomization energies of 12 small molecules (H_2, N_2, O_2, F_2, P_2, Cl_2, HF, CO, H_2O, NH_3, C_2H_2, CH_4) were calculated and compared to their experimental atomization energies as a benchmark. The experimental values were calculated from formation enthalpy data[58] with the experimental zero-point energy[59] removed. Each molecule's bond lengths and angles were set to their experimental values.[59] The RPA correlation energy for each molecule was calculated for each screened cutoff between 10-50 Ryd, with an increment of 1 Ryd, using the two χ^0 construction approaches above. This range of screened cutoffs was chosen to span a wide-range of energies relative to the size of typically chosen SG15 pseudopotential planewave cutoffs.

Figures 4 and S3 summarize the atomization energy mean absolute error (MAE) of the RPA calculations using methods 1 and 2 for χ^0 above, respectively. Each box in these figures shows the atomization energy MAE for the test set in comparison to the experimental reference values for a particular set of correlation energies used in the extrapolation. Each MAE was calculated by: 1) specifying a particular set of $[E_{screen}]$, 2) collecting the corresponding $E_{corr}^{RPA}(E_{screen})$ for all molecules and atomic references, 3) extrapolating each set of values according to Eq. 9 to obtain each $E_{corr}^{RPA,\infty}$, 4) calculating each RPA total energy

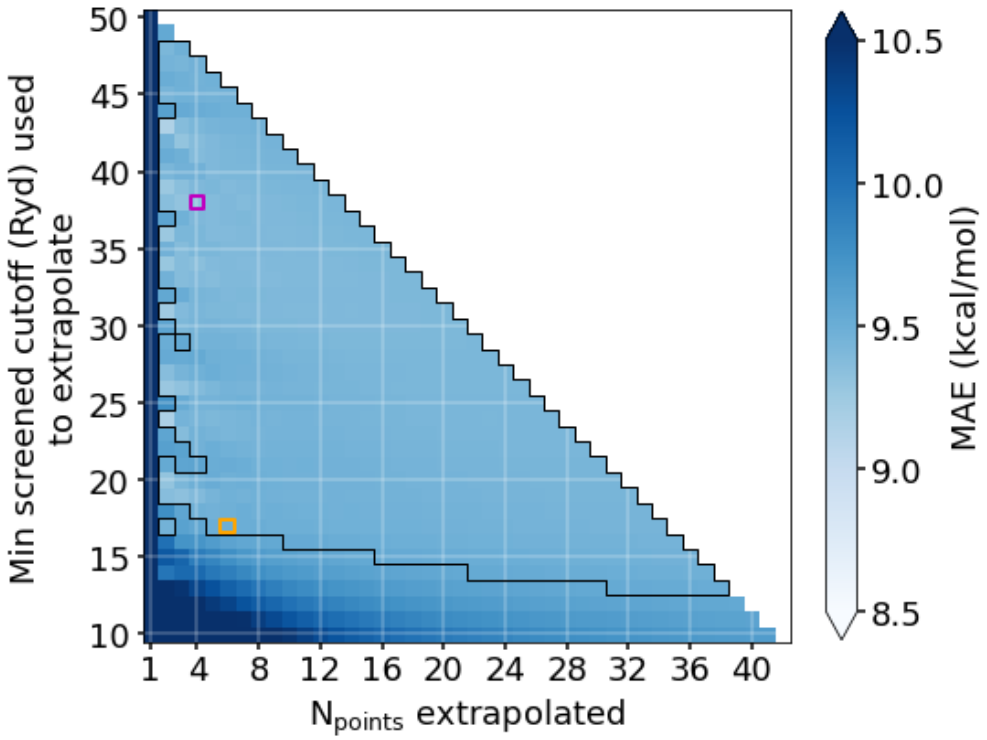

Figure 4: Atomization energy test set MAEs for different RPA correlation energy extrapolations using method 1, as described in the main text, to construct χ^0. Briefly, the number of bands used to construct χ^0 was variable and determined using each screened cutoff. No extrapolation was performed for $N_{points} = 1$. The x-axis denotes how many screened cutoffs and their corresponding RPA correlation energies, $E_{corr}^{RPA}(E_{screen})$, are used to extrapolate for each $E_{corr}^{RPA,\infty}$. The $E_{corr}^{RPA,\infty}$ are then used to calculate the atomization energies. The y-axis denotes the smallest screened cutoff in the $[E_{screen}]$ set. For example, the screened cutoff set [17, 18, 19, 20, 21, 22] Ryd is represented by the point [6, 17], which is the square with an orange border in the figure. The square with the magenta border marks the screened cutoff set that produces the minimum MAE among all sets with $N_{points} \geq 4$ (which was chosen for improved numerical stability in the extrapolation). The boxes within the black border are screened cutoff sets resulting in a MAE within 0.2 kcal/mol of the MAE of the magenta set.

with Eq. 5, and 5) calculating each molecule's atomization energy to use for comparison to experiment. Each set of $[E_{screen}]$ was chosen by sweeping over the 10-50 Ryd screened cutoff range and selecting N_{points} consecutive energies. In the heatmap, each chosen set is labeled on the x-axis by the number of points in the set and on the y-axis by the lowest screened cutoff contained within the set. Overall, both methods produced similar minimum predicted atomization energy MAEs compared to the experimental values. As a result, method 1 was used for all calculations in this work because the smaller χ^0 representation required fewer computing resources for calculating RPA correlation energies.

Extrapolating using RPA correlation energies corresponding to 6 screened cutoff points with a minimum screened cutoff of 17 Ryd (i.e. 17, 18, 19, 20, 21, 22 Ryd) produced an MAE of 9.5 kcal/mol, which was close to the minimum possible MAE for any 6 consecutive screened cutoffs in the set (9.4 kcal/mol for the set starting at 36 Ryd), but at greatly reduced cost due to the cubic increase of the number of unoccupied bands with screened cutoff used to construct χ^0. Summaries of the 17-22 Ryd screened cutoff RPA atomization energies compared to previous studies and experiment are shown in Tables S4 and S5. They are in excellent agreement with Refs. 60, 61, and 62, except for N_2, which here has a 6 kcal/mol smaller atomization energy. We believe the error for N2 originates from the use of norm-conserving pseudopotentials in this work. Ref. 60 discusses uncertainty in RPA correlation energy extrapolations and noted that there is an approximately 2-3 kcal/mol residual uncertainty in their predicted RPA atomization energies using correlation-consistent polarized valence X-tuple zeta basis sets. We note that basis-error-free RPA shows promise for eliminating such uncertainties, as Peng and Ren recently showed in several calculations of benchmark-quality molecular atomization energies.[62] Figure 4 shows a similar range of uncertainties in test set MAE across the entire range of screened cutoffs tested, but also that many screened cutoff sets produce an MAE within 0.2 kcal/mol of each other (shown as the regions enclosed by a black border in Figures 4 and S3) given enough extrapolation points over high enough screened cutoff values, leading to diminishing returns in accuracy

improvement if one extrapolates using more expensive screened cutoff sets.

In addition to the atomization test set, we performed a similar screened cutoff sweep to predict the RPA cohesive energies of 6 solids (AlN zb, InP, MgO, Na, Pd, and Si) and calculated the test set MAEs compared to the set of experimental cohesive energies. Figure S4 summarizes the MAEs calculated for this test set and Table S6 summarizes the MAEs obtained using the 17-22 Ryd screened cutoff RPA correlation energies. These results support those of the atomization energy test set in that one must use enough extrapolation points over high enough screened cutoff values to obtain stable RPA correlation energies. This test set exhibited less MAE dependence on the selection of screened cutoffs however, with nearly all MAE values for $N_{points} \geq 4$ being within 20 meV/atom of each other. Therefore, we used the 17-22 Ryd screened cutoff range to calculate the RPA energies of all other systems studied in this work to maintain consistency across materials classes.

Notably, screened cutoffs of 17-22 Ryd are similar to 50-66% of an assumed 500 eV planewave cutoff for PAW pseudopotentials, which is reasonable because PAWs may not require relatively high planewave cutoffs, such as the value of 60 Ryd (≈816 eV) used here for SG15 pseudopotentials. This observation, along with the good agreement between RPA test set MAEs in Tables S5 and S6, suggests that RPA correlation energy extrapolations are relatively insensitive to pseudopotential choice. We also calculated the PBE and RPA atomization energies using an 80 Ryd planewave cutoff and found that no PBE or RPA atomization energy changed by more than 1 kcal/mol, indicating good convergence with respect to this parameter.

4.3 Impact of the static subspace approximation

In previous work, the static subpsace approximation was shown to efficiently represent the non-interacting electronic polarizability for full-frequency GW calculations for systems without partial occupations and improve computational throughput.[27] As discussed above, we extended this approach to enable full-frequency RPA total energy calculations and GW

calculations with partial occupations at reduced cost. To benchmark the broadening implementations with the subspace code, we calculated the G_0W_0 eigenvalues at high-symmetry points for bulk Cu at its experimental lattice constant and compared to the previous implementation, which used very dense $\mathbf{k}/\mathbf{q}$-grids (16×16×16 to 40×40×40) to sample the Fermi surface without an explicit partial occupation implementation at greatly increased computational expense.[27] Table S7 in the supporting information summarizes these results. Overall, we obtained excellent agreement with previous results given slight differences in DFT calculation methodology. We note that the current implementation helps avoid the need for very dense (e.g. 16×16×16 or denser) $\mathbf{k}/\mathbf{q}$-grid sampling of Fermi level crossings, as the results generated here used a comparatively coarse 12×12×12 $\mathbf{k}/\mathbf{q}$-grid. This $\mathbf{k}/\mathbf{q}$-grid density is consistent with previously reported RPA results for metals[37] and the results discussed in section 4.1.

The RPA correlation energy error due to the static subspace approximation depends on how well the static subspace eigenvalues/vectors, λ_{SS} and $\mathbf{v}_{SS}$, approximate the polarizability for nonzero frequencies. Using fewer eigenpairs will save computational resources but could reduce accuracy. Here, we quantify how different eigenpair selection criteria impact the prediction of materials' RPA correlation energy. The materials test set is described in detail in the Computational Details section, and includes 14 diverse quasi-0D, quasi-2D, and 3D insulators, semiconductors, and metals.

There are many possible approaches to decide whether to retain a particular eigenpair to best represent χ^0. One simple approach retains the i^{th} eigenpair if $|\lambda^{SS}_{i,\mathbf{q}}|/\max(|\lambda^{SS}_{\mathbf{q}}|) \geq \delta_{SS}$, where δ_{SS} is a small positive threshold defined by the user, termed here as the eigenvalue threshold (ET) method. The normalization by the largest eigenvalue helps generalize the approach since different materials have eigenvalues with drastically different magnitudes, as shown in Figure 5. The errors in RPA correlation energy using the ET method for a subset of the tested materials are shown as the dashed lines in Figure 6 for $\delta_{SS} \in \{10^{-2}, 10^{-3}, 10^{-4}, 10^{-5}, 10^{-6}\}$. Results for additional materials are shown in Figure

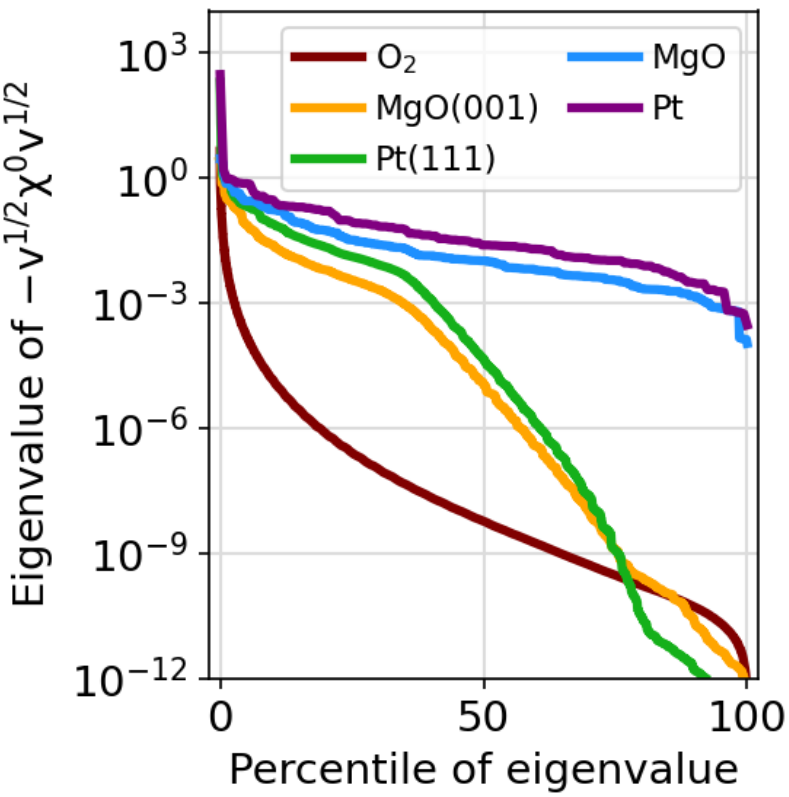

Figure 5: Subspace eigenvalue spectrum sorted by magnitude in descending order for $-v^{1/2}\chi^0 v^{1/2}$ for the **q**-point with smallest magnitude at $\omega = 0$ for a quasi-0D molecule (O_2), quasi-2D surfaces ((1×1) MgO(001) and (1×1) Pt(111)), and 3D periodic materials (MgO and Pt). The max($|\lambda_{SS}|$) for these materials is -4.35, -2.92, -195.56, -2.86, -298.29, respectively. All calculations used a screened cutoff of 20 Ryd. The number of subspace eigenvalues for each system varies with system volume and is 10511, 2457, 1885, 751, and 160, respectively. Figure S5 shows the same data for each eigenvalue index.

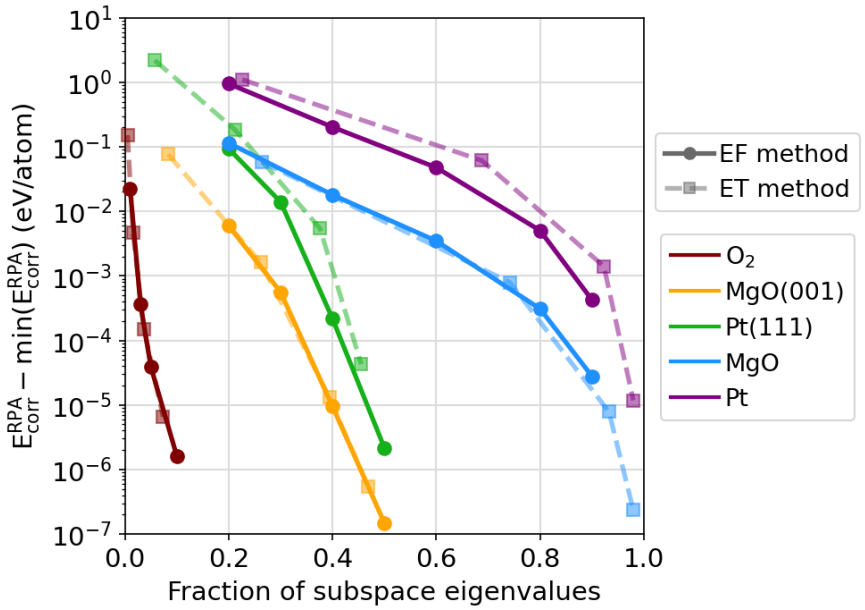

Figure 6: Error in E_{corr}^{RPA} per atom relative to the E_{corr}^{RPA} per atom calculated using the largest number of eigenpairs for either the ET or EF methods as a function of f_{SS} for different materials. All calculations used a screened cutoff of 20 Ryd. Solid (dashed) lines denote RPA correlation energies calculated with the EF (ET) method. From left to right, a quasi-0D molecule, quasi-2D surfaces, and 3D periodic materials need more subspace eigenvalues/vectors to retain the same computational accuracy. For both the EF and ET methods, the $\min(E_{corr}^{RPA})$ point is not shown because it is 0 on the log y-axis. For the ET method, this is the $\delta_{SS} = 10^{-6}$ point. For the EF method, this is the 20, 60, or 100% point for quasi-0D, quasi-2D, or 3D systems, respectively. The errors in the next most stringent calculation of less than 10^{-4} eV/atom indicate that the 20 and 60% points for the low dimensional systems are good approximations of the full basis set calculation.

S6. For the x-axis in Figure 6, the number of eigenpairs retained from application of the ET method were converted into a **q**-point weighted average fraction, f_{SS}, of the total possible χ^0 basis set size defined by the screened cutoff.

However, normalization by $\max(|\lambda_{\mathbf{q}}^{SS}|)$ can be problematic because the ET method may not be expected to perform equally well for both metallic materials and materials with a band gap because as $\mathbf{q} \to 0$, $\lambda_{\mathbf{q}}^{SS}$ can be orders of magnitude larger for metals than for materials with less screening. This results in uneven eigenpair selection across **q**-points. As an alternative, one could select eigenpairs by retaining a user-specified fraction, f_{SS}, of the total basis set space, and thus retaining only the $N_b = f_{SS} N_G$ largest eigenvalues, which are expected to dominate when calculating E_{corr}^{RPA}. We term this the eigenvalue fraction (EF) method. The errors in RPA correlation energy that result from using this approach are shown as the solid lines in Figure 6. Here, $f_{SS} \in \{1, 3, 5, 10, 20\}\%$ for the quasi-0D systems, $f_{SS} \in \{20, 30, 40, 50, 60\}\%$ for the quasi-2D systems, and $f_{SS} \in \{20, 40, 60, 80, 90, 100\}\%$ for the 3D periodic systems.

For both the ET and EF methods, the dimensionality of the material is the primary factor in predicting the error in E_{corr}^{RPA} as opposed to other properties, such as the presence of a band gap for example. The molecular systems converge to a desired accuracy much faster than the 3D periodic materials. However, although either method could be used in practice, the RPA correlation energy for metals converges somewhat faster using the EF method as compared to the ET method. This result also implies that more efficient χ^0 representations should be investigated to further reduce the cost of these calculations. Overall, we find that the EF method yields RPA correlation energy convergence of 1 meV/atom for the molecular, surface, and bulk systems with f_{SS} of 3, 40, and 80%, respectively, with the exception of bulk Pt, which is converged to 5 meV/atom and would require $f_{SS} = 90\%$ instead. Using $f_{SS} = 30\%$ could potentially be used for surfaces as well because the errors of the (1×1) MgO(001), (2×2) 1T-MoS_2, and (1×1) Pt(111) surfaces were only 1, 3, and 14 meV/atom, respectively, which is still relatively small on the scale of catalytic activity. This threshold

could be further lowered if additional accuracy is desired. A higher threshold can be used when taking energy differences, which benefit from error cancellation, as discussed further in section 4.4.

Finally, all of the results discussed above were calculated at a single screened cutoff of 20 Ryd. We performed similar calculations using a second screened cutoff of 10 Ryd because screened cutoff impacts the size of the polarizability and thus the subspace basis set. Comparison of Figures S7 and 6 shows that the fraction of subspace eigenvalues/vectors needed to achieve similar errors in the RPA correlation energy is smaller for the larger screened cutoff. This is simply because the larger screened cutoff increases the basis set size, thus reducing the need to retain as many subspace eigenvalues/vectors. Nevertheless, the 20 Ryd results are more relevant since the optimal extrapolation range is 17-22 Ry (see the discussion in section 4.2). For practical calculations using a screened cutoff extrapolation, we found that the extrapolation substantially reduces the subspace basis set error. Figure S8 shows that for the H_2 molecule, (1×1) Pt(111), and bulk Si, subspace basis set errors of less than 1 meV can be obtained using just 1, 20, and 60% of the possible eigenpairs, suggesting that the above recommendations are likely conservative and could be further lowered. We will discuss error cancellation when calculating adsorption energies in the next section.

4.4 GW/RPA calculations for catalysis

Based on the convergence tests discussed above and those in the Computational Details section, we calculated RPA total energies and GW electronic structures for larger semimetallic and metallic surfaces relevant to catalysis. We calculated the adsorption energies of H and CO adsorbed to (2×2) Pt(111), H and CO adsorbed to the Pt-group metal free (4×6) FeN_4 pyridinic active site embedded in graphene, and H adsorbed to (3×3) 1T-MoS_2. The PBE-relaxed structures of these systems are shown in Figure 7. Table 1 summarizes these results and shows that the adsorption energy of CO is more affected by the use of RPA total energies than the adsorption energy of H. CO can be destabilized by 0.5 eV as compared to DFT.

Notably, we obtain good agreement with literature for the change in CO adsorption energy on Pt(111) due to RPA.[63] RPA correctly predicts the experimentally-observed CO adsorption site ordering, with the atop site being lower in energy than the fcc site, when PBE does not. Lastly, our Pt(111) RPA surface energy is predicted to be 1.00 eV/((111) surface unit area), showing that RPA correctly predicts both the adsorption energy and surface energy.[63] Conversely, we find that H on Pt(111) and FeN_4@G is destabilized by 0.09 and 0.14 eV, respectively, while it is stabilized by 0.5 eV on 1T-MoS_2.

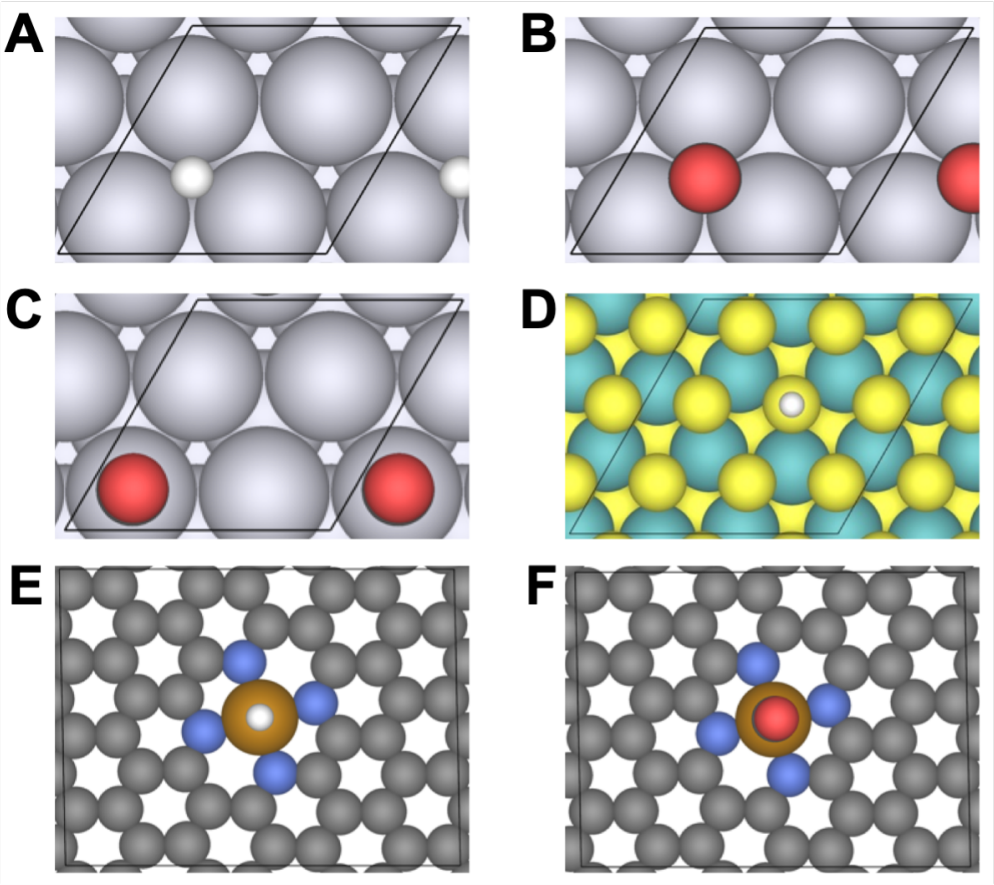

Figure 7: Structures of the (2×2) Pt(111) surface with A) H*, B) CO* at the fcc site, or C) CO* at the atop site, D) (3×3) 1T-phase MoS_2 with H*, (4×6) FeN_4@G with E) H* and F) CO* used for the catalytic GW/RPA calculations. The light gray, white, dark gray, red, teal, yellow, blue, and gold spheres represent Pt, H, C, O, Mo, S, N, and Fe atoms, respectively.

Table 1: Summary of DFT and RPA adsorption energy for the surfaces with H and CO adsorbates. All energies are in eV.

Surface	Ads.	E_{ads}^{DFT}	E_{ads}^{RPA}	$\Delta_{RPA-DFT}$
(2×2) Pt(111)	H	-0.473	-0.387	0.085
(2×2) Pt(111)	CO fcc	-1.657	-1.151	0.506
(2×2) Pt(111)	CO atop	-1.576	-1.391	0.185
(3×3) 1T-MoS_2	H	-1.898	-2.388	-0.490
(4×6) FeN_4@G	H	0.103	0.243	0.140
(4×6) FeN_4@G	CO	-1.348	-0.823	0.525

As discussed above for bulk Cu, our extension of the static subspace approximation for metallic systems further enables its use in GW calculations to complement the study of conducting electrochemical surfaces with RPA total energies. To this end, Figures 8 and S9 show the GW projected density of states for (3×3) 1T-MoS_2+H and (2×2) Pt(111)+CO at the atop site. Both results show a large shift of the bonding H and CO orbitals to energies further below the Fermi level, with smaller shifts of the unoccupied states higher in energy. The changes to the Pt(111)+CO projected density of states results are consistent with those previously studied with GW/RPA.[63]

Next, we determined the computational savings associated with using the subspace approximation for larger system sizes. To do this, we calculated RPA correlation energies for (2×2) Pt(111)+H, (3×3) 1T-MoS_2+H, and (4×6) FeN_4@G+H using the same screened cutoff (20 Ryd) over a wide range of subspace basis set sizes. Table 2 summarizes the time required for these jobs in total GPU-hours. Comparing the 20 and 100% static subspace basis set sizes, the approximation decreased the compute time for the $\chi^0(\omega \neq 0)$ summations by a factor of approximately 20 and the total compute time by a factor of approximately 2-3, with most total time savings happening for the FeN_4@G+H system because it had the largest volume and thus the largest size of χ^0. Reduced time to perform the $\chi^0(\omega \neq 0)$ summations are the dominant contribution to time savings in these calculations. Recent work provides additional information on the parallelization and implementation of the static subspace approach in BerkeleyGW in detail, along with profiling the expected performance

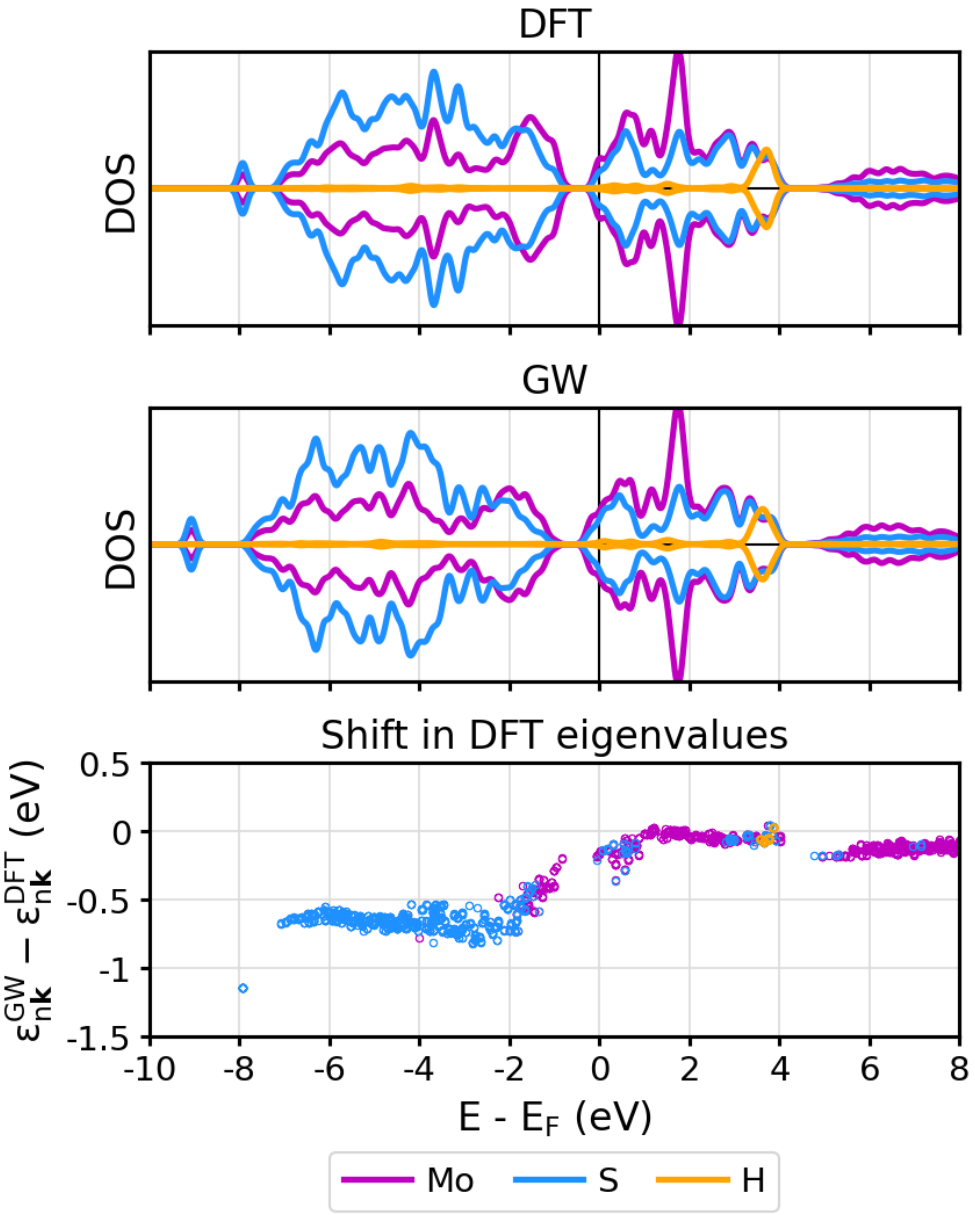

Figure 8: DFT (top) and G_0W_0 (middle) density of states of (3×3) 1T-MoS_2 with H adsorbed at the atop S site. The bottom subplot shows how the DFT eigenvalues (x-axis) shift after the GW calculation. The color of each point was selected by the species associated with the largest magnitude projector for that eigenvalue.

when scaling to very large system sizes with hundreds of atoms.[26]

For these timing calculations, Table S8 summarizes the RPA correlation errors associated with each run. The subspace basis set size errors for these systems were in good agreement with the results discussed in section 4.3, with individual correlation energies converged to better than 1 meV/atom accuracy with 40% of the subspace eigenpairs used. As noted at the end of section 4.3, we again find here that extrapolating to infinite screened cutoff yields subspace basis set errors substantially smaller than the error for a particular finite screened cutoff. For example, for (2×2) Pt(111)+H, the error of the 20% subspace basis correlation energy relative to the 40% subspace basis correlation energy is 1.54 eV, while the error in the extrapolated correlation energy is only -0.05 eV. See Figure S10 for additional details.

Finally, in addition to the above, the error in the predicted RPA correlation energy due to the static subspace approximation (Figure S11) partially cancels for the adsorption energies calculated here due to the similarity between a surface with an open adsorption site and the surface with a bound adsorbate. Figure S12 shows that only 20 and 30% of the subspace eigenpairs are needed for the adsorption energy error to be better than 14 and 0.3 meV, respectively, relative to the 40% subspace basis calculation, even for these larger systems. Altogether, these data suggest that the guidelines in section 4.3 for molecular, surface, and bulk materials can likely be reduced for practical RPA adsorption energy calculations involving extrapolated RPA correlation energies and an energy difference between chemically similar systems. Future studies may obtain additional compute resource savings from even more reduced subspace basis set sizes for their particular application.

5 Conclusions

In this work, we have demonstrated that the static subspace approximation generalized to metallic systems with our approach enables GW/RPA calculations on large unit cells relevant to (electro)catalytic applications. We explored the convergence behavior of RPA

Table 2: Summary of total job time and time for the $\chi^0(\omega \neq 0)$ summations using the static subspace approximation (denoted as $\sum \chi^0_\omega$ in the table). All times are reported in GPU-hours. The calculations for (2×2) Pt(111)+H, (3×3) 1T-MoS_2+H, and (4×6) FeN_4@G+H were all run using a screened cutoff of 20 Ryd and used 40, 24, and 40 NVIDIA H100 GPUs, respectively, on the National Renewable Energy Laboratory Kestrel supercomputer. We note that the number of GPUs was held constant across all subspace basis set sizes to facilitate timing comparisons and that fewer GPUs could have been used for subspace basis set sizes less than 100%. We also note that a single screened cutoff was used only for the timing results in this table to facilitate direct timing comparisons between tests. The energies otherwise reported in this section were calculated with an extrapolation for the RPA correlation energy.

% of subspace	Pt(111)+H time		1T-MoS_2+H time		FeN_4@G+H time	
	$\sum \chi^0_\omega$	Total	$\sum \chi^0_\omega$	Total	$\sum \chi^0_\omega$	Total
10	0.8	41.6	0.7	38.0	1.1	38.6
20	1.8	44.4	1.9	39.7	2.8	41.5
30	3.4	46.3	4.1	44.4	5.4	46.4
40	5.2	49.3	7.0	45.7	9.3	49.6
60	10.3	58.3	15.1	62.6	20.6	65.3
100	38.0	93.8	39.6	95.8	66.5	125.3

total energies with respect to a number of key parameters and quantified the accuracy of the static subspace approximation in predicting RPA total energies with a cost reduction of over an order of magnitude for summations of $\chi^0(\omega \neq 0)$. Using these results, we made recommendations for the application of the static subspace approach to calculations for unexplored materials.

The growing prevalence of GPU supercomputing resources will further enable the use of beyond-DFT methods in the high-throughput exploration of complex interfaces. This work provides insights into the practical challenges associated with using beyond-DFT methods and provides strategies that allow for accurate predictions at reduced cost. Although we focus on surfaces particularly relevant to electrochemistry here, the approach further enables the investigation of other surfaces for other applications that have historically been difficult to study with more computationally-intensive methods like GW and RPA. Additionally, efficient approaches enable much higher calculation throughput. This throughput can be

used for generation of larger data sets to fine-tune foundational machine learning models,[64] a development which could allow for unprecedented descriptions of functional materials in terms of both model complexity and accuracy.

Supporting Information

See the supporting information for tables summarizing additional computational details used for this work, including structure models, spin moments, $\mathbf{k}/\mathbf{q}$-grid samplings, and a detailed description of the quadrature scheme used to evaluate the imaginary frequency integral for RPA correlation energies. Figures showing the complete set of RPA correlation energy convergence results for all tested materials with respect to the number of imaginary frequencies, broadening, screened cutoff, and fraction of subspace eigenvalues are included, along with a figure of $-v^{1/2}\chi^0 v^{1/2}$ values for multiple materials. Additionally, it contains tables listing all calculated molecular atomization energies, solid cohesive energies, and important energies in the bulk Cu electronic structure compared to existing literature[27,37,51,60–62,65,66] and experiment.[58,59] Finally, the supporting information also contains an additional GW projected density of states for (2×2) Pt(111)+CO, a table of RPA correlation energy errors corresponding to the time savings shown in Table 2, and figures showing how the error in RPA correlation energy due to the subspace approximation is decreased by extrapolating the RPA correlation energy to infinite screened cutoff and partially canceled when calculating adsorption energies.

Acknowledgments

This work was primarily supported by the Beyond-DFT Electrochemistry with Accelerated and Solvated Techniques (BEAST) project as part of the Computational Chemical Sciences program, funded by the U.S. Department of Energy, Office of Science, Basic Energy Sciences, award No. DE-SC0022247. M.D.B. acknowledges support by the Center for Computational

Study of Excited-State Phenomena in Energy Materials (C2SEPEM), under contract No. DE-AC02-05CH11231. We used computational resources sponsored by the Department of Energy's Office of Energy Efficiency and Renewable Energy, located at the National Renewable Energy Laboratory; Oak Ridge Leadership Computing Facility at the Oak Ridge National Laboratory, which is supported by the Office of Science of the U.S. Department of Energy under Contract No. DE-AC05-00OR22725; and at the National Energy Research Scientific Computing Center (NERSC), a U.S. Department of Energy Office of Science User Facility located at Lawrence Berkeley National Laboratory, operated under Contract No. DE-AC02-05CH11231 using NERSC award ERCAP-m4025.

Author Declarations

Conflict of Interest

The authors have no conflicts to disclose.

Data Availability

The data that support the findings of this study are available from the corresponding author upon reasonable request.

References

(1) Gonze, X.; Amadon, B.; Antonius, G.; Arnardi, F.; Baguet, L.; Beuken, J.-M.; Bieder, J.; Bottin, F.; Bouchet, J.; Bousquet, E.; Brouwer, N.; Bruneval, F.; Brunin, G.; Cavignac, T.; Charraud, J.-B.; Chen, W.; Côté, M.; Cottenier, S.; Denier, J.; Geneste, G.; Ghosez, P.; Giantomassi, M.; Gillet, Y.; Gingras, O.; Hamann, D. R.; Hautier, G.; He, X.; Helbig, N.; Holzwarth, N.; Jia, Y.; Jollet, F.; Lafargue-Dit-Hauret, W.;

Lejaeghere, K.; Marques, M. A.; Martin, A.; Martins, C.; Miranda, H. P.; Naccarato, F.; Persson, K.; Petretto, G.; Planes, V.; Pouillon, Y.; Prokhorenko, S.; Ricci, F.; Rignanese, G.-M.; Romero, A. H.; Schmitt, M. M.; Torrent, M.; van Setten, M. J.; Van Troeye, B.; Verstraete, M. J.; Zérah, G.; Zwanziger, J. W. The Abinit project: Impact, environment and recent developments. *Computer Physics Communications* **2020**, *248*, 107042.

(2) Kühne, T. D.; Iannuzzi, M.; Del Ben, M.; Rybkin, V. V.; Seewald, P.; Stein, F.; Laino, T.; Khaliullin, R. Z.; Schütt, O.; Schiffmann, F.; Golze, D.; Wilhelm, J.; Chulkov, S.; Bani-Hashemian, M. H.; Weber, V.; Borštnik, U.; Taillefumier, M.; Jakobovits, A. S.; Lazzaro, A.; Pabst, H.; Müller, T.; Schade, R.; Guidon, M.; Andermatt, S.; Holmberg, N.; Schenter, G. K.; Hehn, A.; Bussy, A.; Belleflamme, F.; Tabacchi, G.; Glöß, A.; Lass, M.; Bethune, I.; Mundy, C. J.; Plessl, C.; Watkins, M.; VandeVondele, J.; Krack, M.; Hutter, J. CP2K: An electronic structure and molecular dynamics software package - Quickstep: Efficient and accurate electronic structure calculations. *The Journal of Chemical Physics* **2020**, *152*, 194103.

(3) Enkovaara, J.; Romero, N. A.; Shende, S.; Mortensen, J. J. GPAW - massively parallel electronic structure calculations with Python-based software. *Procedia Computer Science* **2011**, *4*, 17–25, Proceedings of the International Conference on Computational Science, ICCS 2011.

(4) Sundararaman, R.; Letchworth-Weaver, K.; Schwarz, K. A.; Gunceler, D.; Ozhabes, Y.; Arias, T. JDFTx: Software for joint density-functional theory. *SoftwareX* **2017**, *6*, 278–284.

(5) Shao, Y., et al. Advances in molecular quantum chemistry contained in the Q-Chem 4 program package. *Molecular Physics* **2015**, *113*, 184–215.

(6) Giannozzi, P.; Baroni, S.; Bonini, N.; Calandra, M.; Car, R.; Cavazzoni, C.; Ceresoli, D.;

Chiarotti, G. L.; Cococcioni, M.; Dabo, I.; Corso, A. D.; de Gironcoli, S.; Fabris, S.; Fratesi, G.; Gebauer, R.; Gerstmann, U.; Gougoussis, C.; Kokalj, A.; Lazzeri, M.; Martin-Samos, L.; Marzari, N.; Mauri, F.; Mazzarello, R.; Paolini, S.; Pasquarello, A.; Paulatto, L.; Sbraccia, C.; Scandolo, S.; Sclauzero, G.; Seitsonen, A. P.; Smogunov, A.; Umari, P.; Wentzcovitch, R. M. QUANTUM ESPRESSO: a modular and open-source software project for quantum simulations of materials. *Journal of Physics: Condensed Matter* **2009**, *21*, 395502.

(7) Kresse, G.; Hafner, J. Ab initio molecular dynamics for liquid metals. *Phys. Rev. B* **1993**, *47*, 558–561.

(8) Bruneval, F.; Rangel, T.; Hamed, S. M.; Shao, M.; Yang, C.; Neaton, J. B. molgw 1: Many-body perturbation theory software for atoms, molecules, and clusters. *Computer Physics Communications* **2016**, *208*, 149–161.

(9) Deslippe, J.; Samsonidze, G.; Strubbe, D. A.; Jain, M.; Cohen, M. L.; Louie, S. G. BerkeleyGW: A massively parallel computer package for the calculation of the quasiparticle and optical properties of materials and nanostructures. *Computer Physics Communications* **2012**, *183*, 1269–1289.

(10) Govoni, M.; Galli, G. Large scale GW calculations. *Journal of chemical theory and computation* **2015**, *11*, 2680–2696.

(11) Olsen, T.; Patrick, C. E.; Bates, J. E.; Ruzsinszky, A.; Thygesen, K. S. Beyond the RPA and GW methods with adiabatic xc-kernels for accurate ground state and quasiparticle energies. *npj Computational Materials* **2019**, *5*.

(12) Nørskov, J. K.; Rossmeisl, J.; Logadottir, A.; Lindqvist, L.; Kitchin, J. R.; Bligaard, T.; Jónsson, H. Origin of the Overpotential for Oxygen Reduction at a Fuel-Cell Cathode. *J. Phys. Chem. B* **2004**, *108*, 17886–17892.

(13) Ping, Y.; Galli, G.; Goddard, W. A. I. Electronic Structure of IrO_2: The Role of the Metal d Orbitals. *The Journal of Physical Chemistry C* **2015**, *119*, 11570–11577.

(14) Akula, S.; Mooste, M.; Zulevi, B.; McKinney, S.; Kikas, A.; Piirsoo, H.-M.; Rähn, M.; Tamm, A.; Kisand, V.; Serov, A.; Creel, E. B.; Cullen, D. A.; Neyerlin, K. C.; Wang, H.; Odgaard, M.; Reshetenko, T.; Tammeveski, K. Mesoporous textured Fe-N-C electrocatalysts as highly efficient cathodes for proton exchange membrane fuel cells. *Journal of Power Sources* **2022**, *520*, 230819.

(15) Chung, H. T.; Cullen, D. A.; Higgins, D.; Sneed, B. T.; Holby, E. F.; More, K. L.; Zelenay, P. Direct atomic-level insight into the active sites of a high-performance PGM-free ORR catalyst. *Science* **2017**, *357*, 479–484.

(16) Duan, Z.; Henkelman, G. Identification of Active Sites of Pure and Nitrogen-Doped Carbon Materials for Oxygen Reduction Reaction Using Constant-Potential Calculations. *The Journal of Physical Chemistry C* **2020**, *124*, 12016–12023.

(17) Clary, J. M.; Vigil-Fowler, D. Adsorption Site Screening on a PGM-Free Electrocatalyst: Insights from Grand Canonical Density Functional Theory. *J. Phys. Chem. C* **2023**, *127*, 16405–16413.

(18) Tkalych, A. J.; Yu, K.; Carter, E. A. Structural and Electronic Features of β-$Ni(OH)_2$ and β-NiOOH from First Principles. *The Journal of Physical Chemistry C* **2015**, *119*, 24315–24322.

(19) Holby, E. F.; Zelenay, P. Linking structure to function: The search for active sites in non-platinum group metal oxygen reduction reaction catalysts. *Nano Energy* **2016**, *29*, 54–64, Electrocatalysis.

(20) Todorova, T. K.; Schreiber, M. W.; Fontecave, M. Mechanistic Understanding of CO_2 Reduction Reaction (CO_2RR) Toward Multicarbon Products by Heterogeneous Copper-Based Catalysts. *ACS Catalysis* **2020**, *10*, 1754–1768.

(21) Ha, M.-A.; Larsen, R. E. Multiple Reaction Pathways for the Oxygen Evolution Reaction May Contribute to IrO2 (110)'s High Activity. *J. Electrochem. Soc.* **2021**, *168*, 024506.

(22) Shen, H.; Choi, C.; Masa, J.; Li, X.; Qiu, J.; Jung, Y.; Sun, Z. Electrochemical ammonia synthesis: Mechanistic understanding and catalyst design. *Chem* **2021**, *7*, 1708–1754.

(23) Del Ben, M.; Yang, C.; Li, Z.; da Jornada, F. H.; Louie, S. G.; Deslippe, J. Accelerating Large-Scale Excited-State GW Calculations on Leadership HPC Systems. SC20: International Conference for High Performance Computing, Networking, Storage and Analysis. 2020; pp 1–11.

(24) Yu, V. W.-z.; Govoni, M. GPU Acceleration of Large-Scale Full-Frequency GW Calculations. *Journal of Chemical Theory and Computation* **2022**, *18*, 4690–4707, PMID: 35913080.

(25) Deslippe, J.; Samsonidze, G.; Strubbe, D. A.; Jain, M.; Cohen, M. L.; Louie, S. G. BerkeleyGW: A massively parallel computer package for the calculation of the quasiparticle and optical properties of materials and nanostructures. *Computer Physics Communications* **2012**, *183*, 1269–1289.

(26) Weinberg, D.; Hull, O. A.; Clary, J. M.; Sundararaman, R.; Vigil-Fowler, D.; Del Ben, M. Static Subspace Approximation for Random Phase Approximation Correlation Energies: Implementation and Performance. *Journal of Chemical Theory and Computation* **2024**, *20*, 8237–8246, PMID: 39254204.

(27) Del Ben, M.; da Jornada, F. H.; Antonius, G.; Rangel, T.; Louie, S. G.; Deslippe, J.; Canning, A. Static subspace approximation for the evaluation of G_0W_0 quasiparticle energies within a sum-over-bands approach. *Phys. Rev. B* **2019**, *99*, 125128.

(28) Blöchl, P. E.; Jepsen, O.; Andersen, O. K. Improved tetrahedron method for Brillouin-zone integrations. *Phys. Rev. B* **1994**, *49*, 16223–16233.

(29) Choudhary, K.; Tavazza, F. Convergence and machine learning predictions of Monkhorst-Pack k-points and plane-wave cut-off in high-throughput DFT calculations. *Computational Materials Science* **2019**, *161*, 300–308.

(30) Monkhorst, H. J.; Pack, J. D. Special points for Brillouin-zone integrations. *Phys. Rev. B* **1976**, *13*, 5188–5192.

(31) Evarestov, R. A.; Smirnov, V. P. Modification of the Monkhorst-Pack special points meshes in the Brillouin zone for density functional theory and Hartree-Fock calculations. *Phys. Rev. B* **2004**, *70*, 233101.

(32) Methfessel, M.; Paxton, A. T. High-precision sampling for Brillouin-zone integration in metals. *Phys. Rev. B* **1989**, *40*, 3616–3621.

(33) Kratzer, P.; Neugebauer, J. The Basics of Electronic Structure Theory for Periodic Systems. *Frontiers in Chemistry* **2019**, *7*.

(34) Weinberg, D.; Hull, O. A.; Clary, J. M.; Sundararaman, R.; Vigil-Fowler, D.; Del Ben, M. Static Subspace Approximation for Random Phase Approximation Correlation Energies: Implementation and Performance. *Journal of Chemical Theory and Computation* **2024**, *20*, 8237–8246.

(35) Aryasetiawan, F.; Gunnarsson, O. The GW method. *Rep. Prog. Phys.* **1998**, *61*, 237–312.

(36) Fuchs, M.; Gonze, X. Accurate density functionals: Approaches using the adiabatic-connection fluctuation-dissipation theorem. *Phys. Rev. B* **2002**, *65*, 235109.

(37) Harl, J.; Schimka, L.; Kresse, G. Assessing the quality of the random phase approximation for lattice constants and atomization energies of solids. *Phys. Rev. B* **2010**, *81*, 115126.

(38) Sundararaman, R.; Letchworth-Weaver, K.; Schwarz, K. A.; Gunceler, D.; Ozhabes, Y.; Arias, T. A. JDFTx: Software for joint density-functional theory. *SoftwareX* **2017**, *6*, 278–284.

(39) Sundararaman, R.; Arias, T. A. Regularization of the Coulomb singularity in exact exchange by Wigner-Seitz truncated interactions: Towards chemical accuracy in non-trivial systems. *Physical Review B* **2013**, *87*, 165122.

(40) Hybertsen, M. S.; Louie, S. G. Electron correlation in semiconductors and insulators: Band gaps and quasiparticle energies. *Physical Review B* **1986**, *34*, 5390–5413.

(41) Golze, D.; Dvorak, M.; Rinke, P. The GW Compendium: A Practical Guide to Theoretical Photoemission Spectroscopy. *Frontiers in Chemistry* **2019**, *7*.

(42) Adler, S. L. Quantum Theory of the Dielectric Constant in Real Solids. *Phys. Rev.* **1962**, *126*, 413–420.

(43) Wiser, N. Dielectric Constant with Local Field Effects Included. *Phys. Rev.* **1963**, *129*, 62–69.

(44) Johnson, D. L. Local field effects and the dielectric response matrix of insulators: A model. *Phys. Rev. B* **1974**, *9*, 4475–4484.

(45) Hedin, L.; Lundqvist, S. In *Effects of Electron-Electron and Electron-Phonon Interactions on the One-Electron States of Solids*; Seitz, F., Turnbull, D., Ehrenreich, H., Eds.; Solid State Physics; Academic Press, 1970; Vol. 23; pp 1–181.

(46) Wilson, H. F.; Gygi, F. m. c.; Galli, G. Efficient iterative method for calculations of dielectric matrices. *Physical Review B* **2008**, *78*, 113303.

(47) Wilson, H. F.; Lu, D.; Gygi, F. m. c.; Galli, G. Iterative calculations of dielectric eigenvalue spectra. *Physical Review B* **2009**, *79*, 245106.

(48) Nguyen, H.-V.; Pham, T. A.; Rocca, D.; Galli, G. Improving accuracy and efficiency of calculations of photoemission spectra within the many-body perturbation theory. *Physical Review B* **2012**, *85*, 081101.

(49) Pham, T. A.; Nguyen, H.-V.; Rocca, D.; Galli, G. GW calculations using the spectral decomposition of the dielectric matrix: Verification, validation, and comparison of methods. *Physical Review B* **2013**, *87*, 155148.

(50) Schlipf, M.; Gygi, F. Optimization algorithm for the generation of ONCV pseudopotentials. *Computer Physics Communications* **2015**, *196*, 36–44.

(51) Perdew, J. P.; Burke, K.; Ernzerhof, M. Generalized Gradient Approximation Made Simple. *Physical Review Letters* **1996**, *77*, 3865–3868.

(52) Hung, L.; da Jornada, F. H.; Souto-Casares, J.; Chelikowsky, J. R.; Louie, S. G.; Öğüt, S. Excitation spectra of aromatic molecules within a real-space *GW*-BSE formalism: Role of self-consistency and vertex corrections. *Physical Review B* **2016**, *94*, 085125.

(53) Del Ben, M.; da Jornada, F. H.; Canning, A.; Wichmann, N.; Raman, K.; Sasanka, R.; Yang, C.; Louie, S. G.; Deslippe, J. Large-scale GW calculations on pre-exascale HPC systems. *Computer Physics Communications* **2019**, *235*, 187–195.

(54) Altman, A. R.; Kundu, S.; da Jornada, F. H. Mixed Stochastic-Deterministic Approach for Many-Body Perturbation Theory Calculations. *Phys. Rev. Lett.* **2024**, *132*, 086401.

(55) Kresse, G.; Furthmüller, J. Efficient iterative schemes for ab initio total-energy calculations using a plane-wave basis set. *Phys. Rev. B* **1996**, *54*, 11169–11186.

(56) Koch, W.; Holthausen, M. C. *A chemist's guide to density functional theory*; John Wiley & Sons, 2015.

(57) Schmidt, P. S.; Thygesen, K. S. Benchmark Database of Transition Metal Surface and Adsorption Energies from Many-Body Perturbation Theory. *The Journal of Physical Chemistry C* **2018**, *122*, 4381–4390.

(58) Allison, T. C. NIST-JANAF Thermochemical Tables - SRD 13. 2013; `https://janaf.nist.gov/`.

(59) NIST Standard Reference Database Number 101. 2022; `http://cccbdb.nist.gov/`.

(60) Furche, F.; Van Voorhis, T. Fluctuation-dissipation theorem density-functional theory. *The Journal of Chemical Physics* **2005**, *122*, 164106.

(61) Olsen, T.; Thygesen, K. S. Random phase approximation applied to solids, molecules, and graphene-metal interfaces: From van der Waals to covalent bonding. *Phys. Rev. B* **2013**, *87*, 075111.

(62) Peng, H.; Ren, X. *Ab initio* correlated calculations without finite basis-set error: Numerically precise all-electron RPA correlation energies for diatomic molecules. 2024; `https://arxiv.org/abs/2411.01941`.

(63) Schimka, L.; Harl, J.; Stroppa, A.; Grüneis, A.; Marsman, M.; Mittendorfer, F.; Kresse, G. Accurate surface and adsorption energies from many-body perturbation theory. *Nature Materials* **2010**, *9*, 741–744.

(64) Batatia, I.; Benner, P.; Chiang, Y.; Elena, A. M.; Kovács, D. P.; Riebesell, J.; Advincula, X. R.; Asta, M.; Baldwin, W. J.; Bernstein, N.; Bhowmik, A.; Blau, S. M.; Cărare, V.; Darby, J. P.; De, S.; Pia, F. D.; Deringer, V. L.; Elijošius, R.; El-Machachi, Z.; Fako, E.; Ferrari, A. C.; Genreith-Schriever, A.; George, J.; Goodall, R. E. A.; Grey, C. P.; Han, S.; Handley, W.; Heenen, H. H.; Hermansson, K.; Holm, C.; Jaafar, J.; Hofmann, S.; Jakob, K. S.; Jung, H.; Kapil, V.; Kaplan, A. D.; Karimitari, N.; Kroupa, N.; Kullgren, J.; Kuner, M. C.; Kuryla, D.; Liepuoniute, G.; Margraf, J. T.; Magdău, I.-B.; Michaelides, A.; Moore, J. H.; Naik, A. A.; Niblett, S. P.;

Norwood, S. W.; O'Neill, N.; Ortner, C.; Persson, K. A.; Reuter, K.; Rosen, A. S.; Schaaf, L. L.; Schran, C.; Sivonxay, E.; Stenczel, T. K.; Svahn, V.; Sutton, C.; van der Oord, C.; Varga-Umbrich, E.; Vegge, T.; Vondrák, M.; Wang, Y.; Witt, W. C.; Zills, F.; Csányi, G. A foundation model for atomistic materials chemistry. **2023**,

(65) Paier, J.; Hirschl, R.; Marsman, M.; Kresse, G. The Perdew–Burke–Ernzerhof exchange-correlation functional applied to the G2-1 test set using a plane-wave basis set. *The Journal of Chemical Physics* **2005**, *122*, 234102.

(66) Olsen, T.; Thygesen, K. S. Accurate Ground-State Energies of Solids and Molecules from Time-Dependent Density-Functional Theory. *Phys. Rev. Lett.* **2014**, *112*, 203001.

Table of Contents Figure